SAND2014-17433C

Investigations of Closely Coupled Pilot and Main Injections as a Means to Reduce Combustion Noise

Stephen Busch[1], Kan Zha[1], Paul C. Miles[1]

[1]Sandia National Laboratories, Engine Combustion Department; PO Box 969, MS 9053; Livermore, CA 94551-0969

E-mail: sbusch@sandia.gov
Telephone: +1-925-294-2216
Fax: +1-925-294-1004

Abstract:

Various pilot-main injection strategies are investigated in a single cylinder optical Diesel engine. With a pilot injection that is advanced from the main injection by 300 μs or more, a 9 dB reduction in combustion noise is achieved. It is observed that as the dwell between a single pilot and the main injection is decreased towards zero, combustion noise passes through a minimum and a further reduction of 3 dB is possible. This additional decrease in combustion noise is not associated with increases in smoke or NO_x emissions. The injection schedules employed in the engine are analyzed with a hydraulic injection analyzer to provide rate shapes for each of the dwells tested. Two distinct injection events are observed even at the shortest dwell tested, and various rate shaping effects are observed with the main injection event as the dwell is adjusted. High-speed elastic scattering imaging of liquid fuel is performed in the engine to examine initial spray penetration rates; these are compared to the measured rates of injection. The penetration rate results provide evidence that rate shaping of the initial phase of the main injection is occurring in the engine and that this rate shaping is consistent with the injection rate data. Although changes in the main injection rate are believed to occur in the engine, experimental evidence suggests that these changes are not responsible for the observed trend in combustion noise as dwell changes. The combination of thermodynamic data and rate of injection data support the theory that the main injection interacts with the pilot mixture field and influences its combustion, thus playing a role in decreasing combustion noise. The relative phasing of the pilot and main heat release may play a significant role in reducing combustion noise; further studies will focus on combustion phasing effects.

Nomenclature

AHRR	Apparent heat release rate
ASSE	After the start of solenoid energizing
ATDC	After top dead center
CAD	Crank angle degrees
COV	Coefficient of variation
δt	Energizing dwell
ET	Energizing time
FIR	Finite impulse response
FSN	Filter smoke number
HDA	German acronym: Hydraulischer Druckanstieg (hydraulic pressure increase)
ID	Ignition delay
$IMEP_g$	Gross indicated mean effective pressure
m_{pilot}	Pilot injection quantity
SOC	Start of combustion
SOI_{pilot}	Start of pilot injection
SSE	Start of solenoid energizing
TDC	Top dead center
UHC	Unburned hydrocarbons

1. Introduction / Motivation

To improve customer acceptance and reduce noise pollution, it is desirable to make automotive Diesel engines quieter. Pilot injections have long been used in direct injection Diesel engines as a means to reduce combustion noise (Russell *et al.*, 1993; Dürnholz *et al.*, 1994). The mechanism by which noise is reduced is as follows: the heat released by the pilot fuel increases temperatures and radical concentrations within the cylinder and therefore decreases the ignition delay of the fuel injected during the main injection. Combustion of the main injection is therefore predominantly mixing-controlled and characterized by lower rates of heat release than for premixed combustion. The relatively small amount of pilot fuel, combined with the interruption in the rate of injection, results in a smaller amount of premixed combustion than for a single injection. In this way, combustion noise is suppressed through the use of a pilot. Advances in fuel injection hardware, such as common rail systems and fast response injectors, have made multiple injection strategies robust and effective. Piezo injectors are well known for their precision and short reaction times, but state-of-the-art solenoid injectors can reliably deliver up to eight injections per cycle with very short separation times between injection events (Fiat, 2009). Split armature modules enable closely spaced injections and even zero hydraulic dwell (delay) between injection events and thus injection rate shaping (Bosch, 2011; Fiat, 2009).

Dürnholz *et al.* investigated the effects of a pilot injection on combustion noise, fuel economy, and emissions with various pump-line-nozzle injector configurations in a passenger car Diesel engine (1994). Their injection system made it possible to vary the quantity, timing, and rate of the pilot injection. For an engine speed of 2000 rpm and a “medium” load, combustion noise depended strongly on the pilot quantity; minimal combustion noise levels were achieved with a pilot quantity of between 2 and 3 mm^3/str. The noise minimum corresponds to a minimum in ignition delay for the main injection, and to approximately 8% of the fuel being burned before the start of the main injection. Measured combustion noise was always lower with a pilot than without, but the noise increased for hydraulic dwells (injection interrupt durations) shorter than approximately 12 °CA (1000 µs at 2000 rpm).

Badami *et al.* performed investigations using a common rail system with solenoid injectors in a passenger car Diesel engine (2001). They examined three different operating points with pilot-main injection strategies and varied pilot injection quantity and energizing dwell at each point. At a fixed load, pilot injection quantity affected not only the combustion noise at a given energizing dwell, but also the trend in combustion noise with changing dwell. Moreover, trends in combustion noise for different operating points were quite different for a given pilot injection quantity. At moderate engine loads (bmep/n: 5 bar/1500 rpm and 8 bar/2000 rpm), combustion noise sometimes changed dramatically for energizing dwells shorter than 500 µs. At the highest load tested (8 bar/2000 rpm) and for the larger pilot injection quantities tested, combustion noise was observed to decrease dramatically at the shortest energizing dwells (near 86 µs). Badami *et al.* show that by varying only the dwell for a given pilot injection quantity, combustion noise can vary by as much as 3 dB; this is equivalent to a factor of 2 in acoustic power.

Ricaud and Lavoisier optimized multiple injection settings in a single-cylinder, small-bore engine with a piezoelectric injector for several multiple injection strategies (2002). Dwell and quantity were varied for each injection event, as well as the start of the main injection, the rail pressure, and the EGR rate. For a pilot-main injection strategy, combustion noise varied significantly as dwell and pilot injection quantity were changed. Furthermore, the pilot fuel quantity resulting in the lowest combustion noise level depended on the dwell. The noise-optimal pilot injection quantity was smallest for intermediate dwells. For noise-optimized operation, peak heat release rates are the same for the pilot and the main combustion events. This observation was made for several operating points, and it was suggested that the noise-optimized settings are a balance between excessive pilot heat release and excessive main combustion heat release.

Properly applied multiple injection strategies can be beneficial for combustion noise, fuel consumption, and pollutant emissions, and are therefore a powerful tool. However, with so many calibration parameters, including injection and dwell durations for each injection event; rail pressure; and injection train phasing; developing engine calibrations over the entire operating map is a complicated and time consuming process. A particular injection train may yield minimal combustion noise for a given operating point, but it may not be obvious why these parameters are optimal or why different parameters are necessary for a different operating point. Without a detailed understanding of the mechanisms by which noise can be decreased with multiple injections and closely coupled pilot injections, it will be difficult to reduce the amount of effort necessary to develop and optimize such calibrations. The goal of this work is to provide insight into the interactions between the pilot and main injections within the injector and within the cylinder, and increased understanding of how combustion noise is impacted by these interactions.

In this study, a pilot-main injection strategy is investigated at moderate load in an optical small-bore Diesel engine. The pre-production injector used is a fast-acting, pressure-balanced, solenoid-actuated injector, which enables very closely coupled injection events. Engine testing is performed for a dwell sweep at a moderate load, and trends in exhaust emissions, heat release rates, and combustion noise are measured. The injection schedules used in the engine testing are measured with a hydraulic injection analyzer to provide rate shapes for each of the dwells tested. High speed elastic scattering images are taken in the engine to provide information about the liquid fuel as it is injected into the cylinder. The comparison between the rate shape data and liquid penetration data provide information about the changes in the rise rate of the main injection as dwell changes. The combination of rate shape and thermodynamic data provides evidence of the interaction between the main injection and the pilot mixture field.

2. Experimental Setup

2.1. Engine and Fuel Injector

The single-cylinder optical Diesel engine used in this study is based on a modified 1.9 L GM four valve head. The main geometric specifications are provided in Table 1. The engine features a Bowditch-style piston, which is fitted with a titanium piston top for the cylinder-pressure based and emissions measurements; and with a fused-silica piston top for the optical investigations described below. The geometrically identical piston tops feature a reentrant bowl and valve cut-outs.

Table 1: Engine geometry and fuel properties

Engine Geometry		
Valves	[-]	4
Bore	[mm]	82
Stroke	[mm]	90.4
Displacement Vol.	[L]	0.477
Geometric CR	[-]	16.69

Fuel
42 vol% n-$C_{16}H_{34}$; 58 vol% iso-$C_{16}H_{34}$

Optical access through the sides of the combustion chamber is provided by fused silica windows (50 mm wide by 25 mm tall) located at the top of the cylinder liner. These windows are positioned to allow unobstructed optical access into the clearance volume, even when the piston is located at TDC. The engine is equipped with a Kistler 6125b pressure transducer mounted in the location of the production engine glow plug, and the in-cylinder pressure is acquired every 0.25° crank angle (CA).

The injector used in this study is a pre-production solenoid injector, which is equipped with a pressure-balanced nozzle control valve to enable very closely spaced injection events. The mini sac nozzle has equally spaced holes with exit diameters of 139 µm and conicity of 1.5; the included angle of the holes is 149°. Flexible control of solenoid energizing durations (referred to as ET) and energizing dwells is provided by a Genotec injector controller. For this study, dwell refers to the time between the end of the pilot energizing signal and the beginning of the main energizing signal (see Fig. 1). The dwell is varied between 80 and 1200 µs.

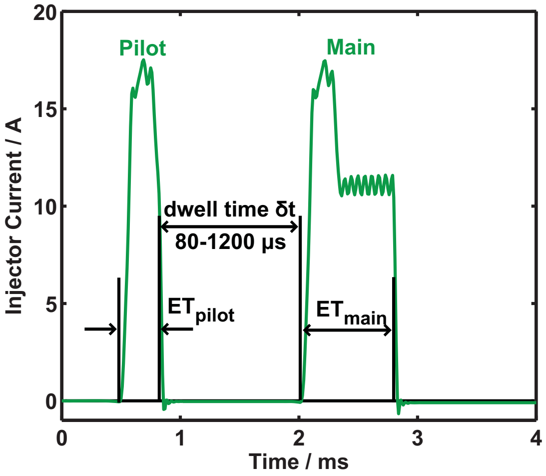

Fig. 1: injector solenoid energizing and dwell definition

2.2. HDA

The Moehwald HDA (HDA is a German acronym for hydraulic pressure increase: Hydraulischer Druckanstieg) is a commercially available injection rate and mass measurement device that utilizes the change in hydraulic pressure that results from injecting fluid into a closed, fluid-filled chamber. It is essentially an evolution of Zeuch's original measurement device (1961). The underlying measurement principle relies on both the measured pressure in a constant-volume chamber and the speed of sound of the fluid within the chamber. With the assumption of a reversible, adiabatic (isentropic) injection into the chamber, the injection mass flow rate can be expressed as follows:

$$\frac{dm}{dt} = \frac{V\frac{dP}{dt}}{\frac{dP}{d\rho}} = \frac{V}{c^2}\frac{dP}{dt}, \qquad (1)$$

where:

m is the mass of fluid in the chamber,
V is the volume of the chamber,
t is time,
P is the chamber pressure, and
ρ is the fluid density
c is the speed of sound in the fluid

Integration of equation (1) between two points in time (and thus two discrete pressures) yields a cumulative mass:

$$m_{1-2} = \int_{\tau_1}^{\tau_2} \frac{dm}{dt} dt = V \int_{P_1}^{P_2} \frac{1}{c(P(t))^2} \frac{dP}{dt} dP \qquad (2)$$

So, for a given chamber volume, the mass flow rate and cumulative mass can be determined if the time-dependent pressure and pressure-dependent speed of sound are known. Whereas Zeuch assumed a constant value for the compressibility of his fuel (1961), in the HDA the speed of sound is measured directly. Hence, uncertainties in fluid properties such as density and bulk modulus do not adversely affect the accuracy of the results.

A schematic diagram of the HDA setup is shown in Fig. 2. A PC is used to communicate with the injector driver and the HDA control module. Fuel is supplied by a small feed pump to a high pressure, three-piston pump, after which it flows into a production common rail. Rail pressure is controlled via modulation of the metering valve in the CP1. A PC is used to communicate with the injector driver and the HDA control module. The configuration of the fuel injection hardware is essentially unchanged from the setup used for engine testing.

The HDA's cylindrical chamber has a volume of 128 ml, and its walls are temperature controlled via an external heated recirculator that pumps heat transfer fluid through the chamber walls. A piezoresistive pressure sensor is mounted in the cylinder wall halfway between the top and the bottom of the chamber. The pressure signal is passed through an analog anti-aliasing filter with a cutoff frequency of 25 kHz before being digitized with 16-bit resolution at a rate of 100 kHz. Additional digital processing of the pressure signal accounts for the temperature dependence of the pressure sensor sensitivity, as well as nonlinearities in the sensor output. Finally, the pressure signal is digitally filtered using a raised-cosine, finite-impulse-response (FIR) filter with a cutoff frequency of 10 kHz. In addition to the injection rate, the solenoid current is measured using a Pearson Model 411 Current Monitor placed around the injector cable and digitized at 100 kHz.

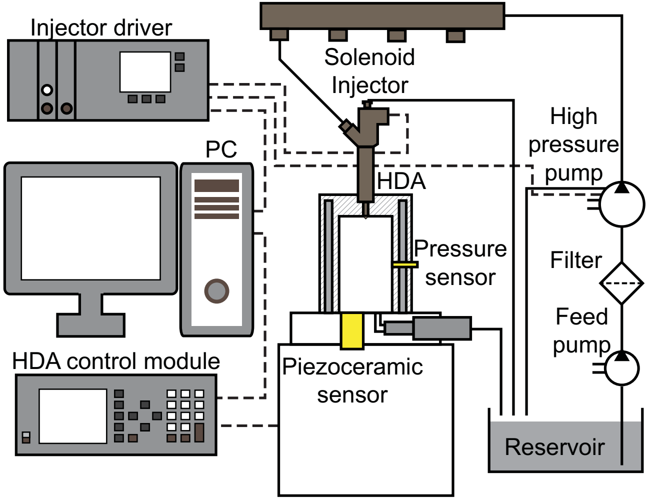

Fig. 2: Setup of the HDA and auxiliary components

To measure the speed of sound, an electronic pulse is sent to a piezoceramic sensor, which creates a pressure wave that travels through the fluid in the chamber, is reflected at the top of the chamber, and detected by the same sensor upon its return. A clock speed of 75 MHz yields a timing resolution of 13.33 ns, and quantization noise is reported to be on the order of 0.1 m/s (Moehwald, 2008). Neglecting any uncertainty in the chamber height, the total uncertainty in the speed of sound is estimated to be 0.25 m/s, which is typically less than 0.025% of the measured value.

The analysis of multiple cycles yields statistical information about a particular set of operating conditions. This includes the mean and the standard deviation of the injected mass, among other quantities. For the current work, no systematic difference was observed between the mean values and standard deviations when the statistics were taken over either 50 or 100 cycles. For this reason, each data point presented in this paper represents the ensemble average of 50 injections. Hydraulic starts of injection are identified by the positive-sloped zero crossings observed at the beginning of each injection event.

2.3. Engine Operating Conditions and Procedure

Initial testing was performed with the metal piston to characterize the operation of the engine as dwell is varied. For these tests, the engine was operated with a constant engine speed, $IMEP_g$, injection pressure, and pilot injection quantity (see Table 2). The engine was operated in skip-fire mode; fuel was injected in every fifth cycle. The main injection duration was adjusted to maintain the engine load ($IMEP_g$), and the injection train was block-shifted to achieve a near-constant 50% mass fraction burned angle of 13 °CA ATDC. The intake mass flow rate was held constant throughout the testing and resulted in a motored TDC density of approximately 21.8 kg/m^3. EGR was simulated by replacing intake air with a mixture of nitrogen and CO_2 and matching the total mass in the cylinder to the mass that would be present with real EGR. The residual fraction that would be expected in a continuously fired metal engine was also simulated in this manner. Exhaust emissions (NO_x, smoke number, CO, and UHC) were measured during skip-fired operation and corrected to represent emissions levels obtained in continuously-fired operation. For each operating point, the engine was motored for approximately 90 seconds to allow the intake and exhaust pressures to stabilize. An emissions measurement was taken just before the engine was skip-fired, and a second emissions measurement was taken after approximately 60 seconds of skip-fired operation and averaged over 20 seconds of operation.

After the initial engine testing, the injector was tested in the HDA. Rates of injection were measured for the injection schedules developed during the engine testing, among others. The HDA chamber pressure was set to be consistent with the cylinder pressure at the time of injection. Fuel and chamber temperatures were held constant at 90°C, although measured rates of injection are not sensitive to fuel temperature at temperatures above 60°C. The injector was then reinstalled in the engine and the fused silica piston top was installed. Intake air mass flow was replaced with pure nitrogen to prevent combustion and the associated window fouling. Four of the injection trains developed in fired operation were used for the optical measurements.

For each fired operating point, combustion noise is calculated from 50 cycles' worth of raw cylinder pressure data according to the routine provided in (Shahlari *et al.*, 2013), which is similar or identical to the routines used by commercial devices to compute combustion noise. The average of these 50 values is reported here for each case. Apparent heat release rate (AHRR) is computed with an iterative, two-zone model, in which temperature and composition dependent gas properties are taken into account. Heat transfer and crevice flow effects are partially compensated by subtracting the AHRR of a motored pressure trace from the AHRR of the fired trace. A cosine-symmetric low pass FIR filter is used to smooth the fired cylinder pressure traces before the AHRR is calculated. Its pass band edge is located at 5 kHz. This preserves the frequency content of the cylinder pressure traces in the frequency bands most relevant to combustion noise. The AHRR traces shown in this work are ensemble averaged over 50 fired cycles.

Table 2: Engine operating parameters

Engine speed	[rpm]	1500
Swirl ratio (Ricardo)	[-]	2.2
$IMEP_g$	[bar]	9.0 ± 0.1
Injection pressure	[bar]	800
m_{Pilot}	[mg/str]	1.5
Dwell time δt for initial testing (δt…step size…δt)	[µs]	0 (no pilot) 80…*20*…200 300…*100*…500 600…*200*…1200
Dwell time δt for optical measurements	[µs]	0, 90, 140, 300
Intake temperature	[K]	347.15
TDC temperature	[K]	925
TDC density	[kg/m^3]	21.8
EGR	[%]	10.3 (includes 3.3% residual fraction)
MFB50	[CAD ATDC]	13 ± 0.5

2.4. Optical setup

An elastic scattering imaging technique was developed to provide temporally and spatially resolved information about the fuel injection process for several dwells. Imaging was performed with a Photron SA-X2 monochromatic CMOS camera at a rate of 120 kfps. For a constant engine speed of 1500 rpm, this equates to a crank angle resolution of 0.075 CAD. Images were captured through the fused silica piston with a 105 mm focal length f/3.5 Nikkor lens. The cylinder head and valves were airbrushed with a thin coat of matte black heat resistant paint to minimize reflections. A high repetition rate, high intensity, short-pulse LED illumination system was employed to provide sufficient image intensities at these high frame rates. A red LED with a 3x3 mm^2 chip proved to be robust and sufficiently bright with pulse widths of 1.5 µs and peak forward currents exceeding 45 A. The LED pulses were timed so that each camera frame is exposed for the entire LED pulse duration. A system of three plano-convex lenses was developed to increase the amount of light that was passed into the cylinder. The setup in the test bench including the "focusing optics" is depicted in Fig. 3, along with an example of a raw image.

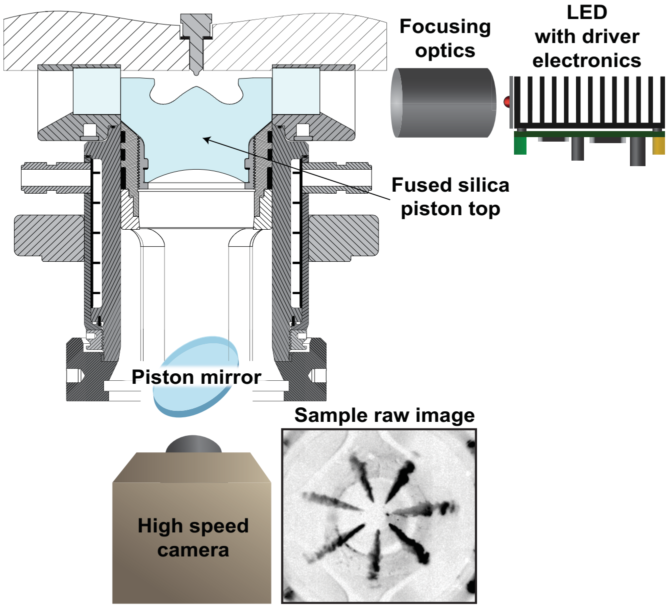

Fig. 3: Setup for high speed elastic scattering imaging and sample raw image (inverted grayscale color map, 0-512 counts, gamma = 0.7)

The LED and its lens system were positioned outside of the liner window on the intake side of the engine. The incoming light is scattered by the strong density gradients at the fuel jets, and the angle of incidence relative to the jet axis is different for each jet. This non-axisymmetric illumination complicates the image analysis, but each jet is treated independently in the image processing. Errors associated with non-uniform illumination are negligible in comparison to the changes observed with changing dwell. The trigger to start acquiring images is the signal used to trigger the injector driver to start injecting, i.e. it occurs at the start of solenoid energizing (SSE). In each injected cycle, 300 images are taken to capture the entire pilot and main injection events. Images are taken for 45 consecutive (skip-fired) cycles for each dwell tested.

The raw images are distortion corrected with an automated routine based on ray tracing, background subtracted, and thresholded before starts of injection, liquid lengths, and penetration rates are computed from them. These procedures are described in the Appendix, where an example of a processed image is also shown.

3. Results

As described above, initial investigations are performed with the metal piston top and with fired operation. Dwell is varied from 80 µs to 1200 µs, and a single injection serves as a reference. The resulting trend in combustion noise is shown in Fig. 4 for two runs, but experiments have also been performed with a second, nominally identical injector, and the results are closely repeatable. Standard deviations for a given dwell are typically less than 0.4 dBA. Although the highest standard deviations typically occur for dwells of less than 200 µs, they are often comparable to the standard deviation for a single injection. The single injection case is shown in this work as a dwell of zero.

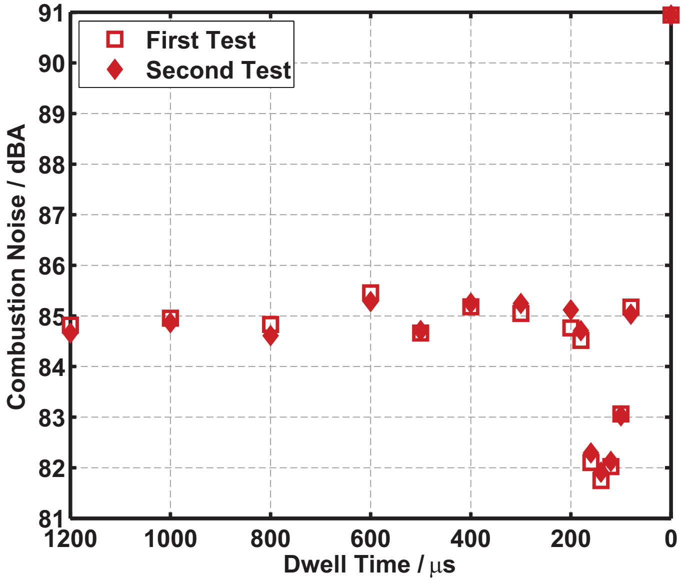

Fig. 4: Combustion noise vs. dwell for the pilot-main injection strategy

The use of a pilot injection significantly decreases noise levels below the level obtained with a single injection: for dwells longer than 200 μs this reduction is approximately 6 dB. However, a further decrease in combustion noise is observed as the dwell decreases below 200 μs, and the minimum occurs at a dwell of 140 μs. The minimum noise levels are approximately 3 dBA below the levels obtained with longer dwells; 3 dB corresponds to a factor of two in terms of acoustic power. Understanding the causes of this noise minimum is the goal of this research project. For dwells shorter than 140 μs, combustion noise levels again increase, and for a dwell of 80 μs, combustion noise levels are close to the 85 dBA level that is measured for longer dwells. For all dwells tested, the COV of IMEP_g remains below 2.5%, but the COV values are typically slightly higher at dwells near 140 μs than for other dwells. Normalized indicated specific exhaust emissions and filter smoke numbers for these tests are shown in Fig. 5; they have been normalized by the levels measured for the single injection case.

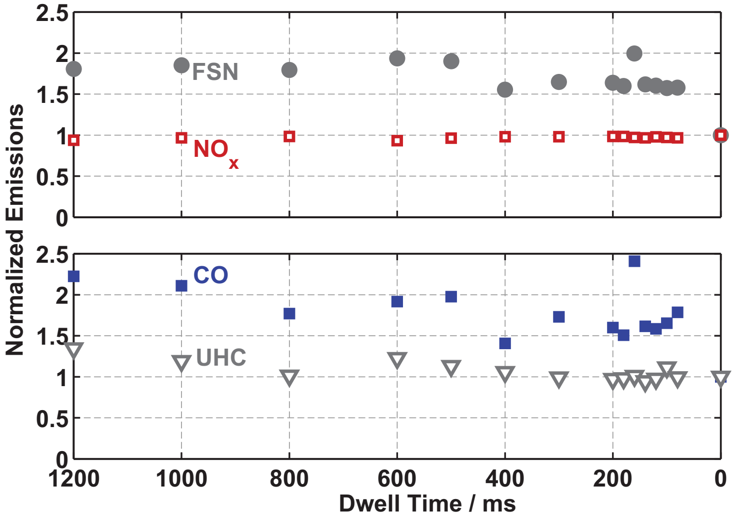

Fig. 5: Normalized exhaust emissions: FSN, NO_x, CO, and UHC vs. dwell

For this operating point, NO_x emissions are highest with a single injection, but only slightly lower with a pilot injection. They do not change significantly as dwell changes. FSN levels are higher with a pilot injection than without. Local maxima in FSN occur at dwells of 600 μs and 160 μs. The behavior in FSN at dwells less than 200 μs is not always repeatable: local maxima appear at different dwells and their magnitudes vary from test to test, but local maxima in FSN values are never observed for a dwell of 140 µs. Higher FSN levels are typically associated with higher CO levels, which suggests that the rich mixtures responsible for the formation of soot may also be responsible for the formation of excess CO. Unburned hydrocarbon (UHC) levels are generally low; they correspond to approximately 0.1% of the injected fuel mass. For shorter dwells, UHC levels are most similar to those obtained with a single injection. Note that the noise minimum seen in Fig. 4 at a dwell of 140 µs occurs without penalties in pollutant emissions (when compared to other dwells). This trend has been observed in repeated emissions tests.

Each injection schedule developed during the fired tests has been measured outside of the engine with the HDA. Because the injector solenoid current is measured both in fired engine operation and with the HDA, the measured injection rates can be synchronized with the measurements taken in the engine (engine speed is assumed to remain constant throughout the portion of the cycle during which the injection occurs). Rates of injection are shown together with calculated apparent heat release rate (AHRR) data for several dwells and for the single injection case in Fig. 6. At this point, it is assumed that the rates of injection measured with the HDA represent those obtained with fired engine operation.

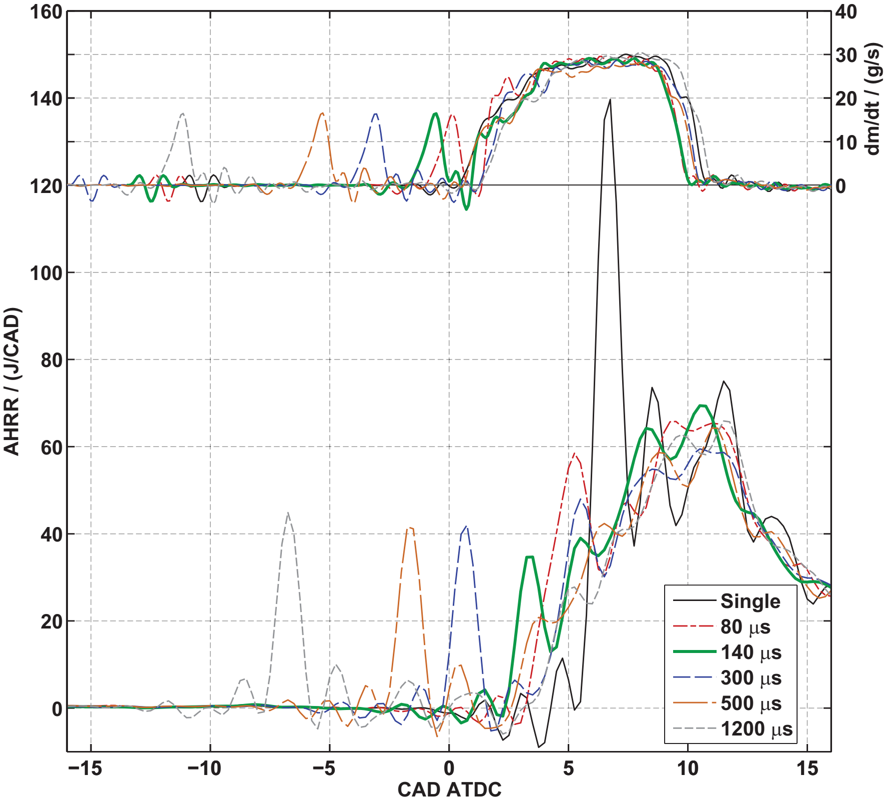

Fig. 6: Rates of injection (top) and AHRR data (bottom) for several dwells and the single injection case

As the dwell changes, the phasing of the injection train is adjusted to maintain combustion phasing (as indicated by MFB50). The timing of the main injection changes much less than the timing of the pilot injection as the dwell is changed. For a dwell of 1200 µs, the heat release associated with the pilot injection occurs before the start of the main injection. The same is largely true for a dwell of 500 µs, as well. However, for a dwell of 300 µs, the main fuel injection begins as the pilot heat release is finishing. For dwells shorter than this, the main injection overlaps with the pilot heat release. Peak apparent heat release rates for the pilot mixture are typically slightly higher than 40 J/ CAD for dwells of 300 µs and longer. However, as the dwell decreases below 300 µs, the peak apparent pilot heat release rate decreases and reaches a minimum at a dwell near 140 µs. After this, it becomes difficult to distinguish the heat release attributed to the pilot injection from that attributed to the main injection, even though two distinct injection events are observed even for a dwell of 80 µs. The AHRR curve for a dwell of 80 µs indicates that the initial heat release peak is larger than the pilot heat release peaks observed for longer dwells. For this operating point, the pilot injection decreases peak heat release rates below the single injection levels by a factor of more than two. The differences in AHRR traces are most pronounced during the early stages of combustion; after approximately 10 CAD ATDC, it is difficult to distinguish between the various AHRR curves.

In a separate test, the start of the main injection as detected by the HDA was held constant for a variety of dwells; the trend in combustion noise was essentially unchanged.

Based on the type of data shown in Fig. 6, an ignition delay (ID) can be defined based on the detected start of pilot injection and the calculated start of apparent heat release. The start of the pilot injection is defined as the last zero crossing of the rate of injection curve before the pilot injection is clearly detected. The start of combustion is defined as the last zero crossing before the first significant peak in the AHRR signal. For longer dwells, this is attributed to the combustion of the pilot injection, but for very short dwells, it is unclear if the heat release is due only to the pilot or if combustion of the main injection begins at the same time. In this case and in the case of a single injection, the start of combustion simply refers to the start of measurable heat release. The start of pilot injection and start of combustion are illustrated in Fig. 7 for a dwell of 300 µs. SOI_{pilot}, SOC, and ID are shown in Fig. 8 for all dwells tested.

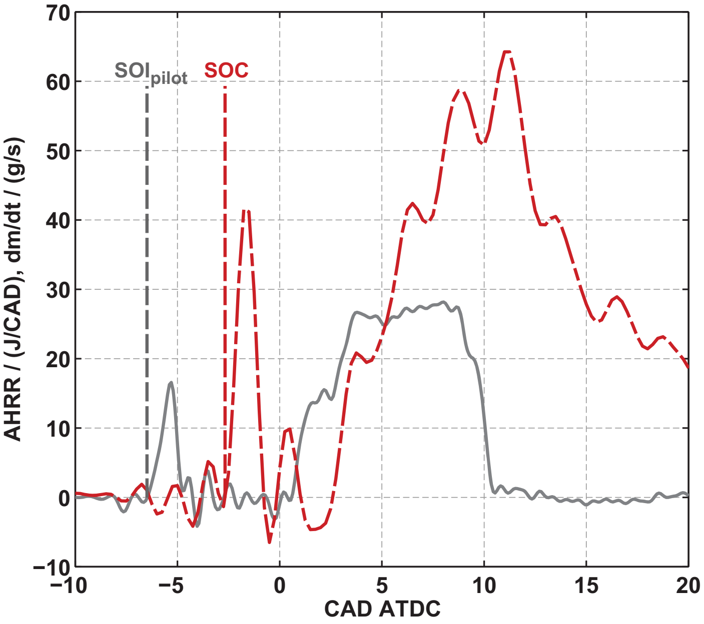

Fig. 7: Definition of start of injection for the pilot injection (SOI_{pilot}) and the start of combustion (SOC)

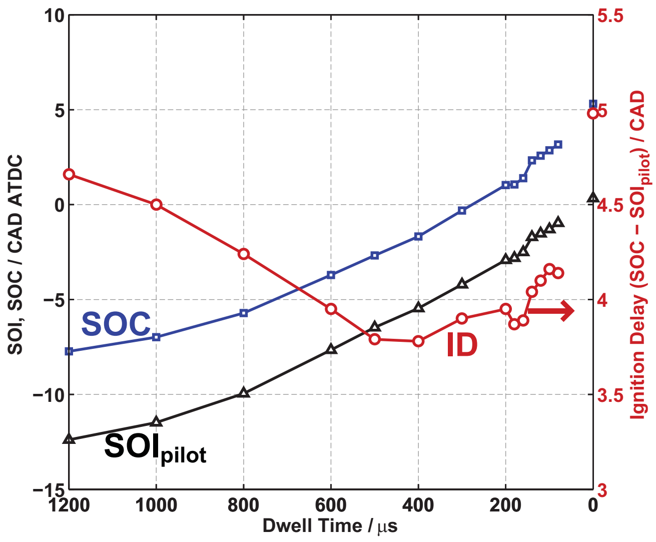

Fig. 8: Start of pilot injection (SOI_{pilot}), start of combustion (SOC), and ignition delay (ID) vs. dwell (single injection shown at zero dwell)

The ignition delay obtained with a single injection is longer than the ignition delay obtained with a pilot injection regardless of dwell. The pilot injection timing is dictated by the dwell, the pilot injection energizing time, and the desired CA50. As mentioned above, the timing of the main injection does not change significantly for these tests, so the trend in SOI_{pilot} is logical. As dwell increases above 400 μs, the pilot fuel is injected into an increasingly cooler environment, so the ignition delay becomes longer. For dwells shorter than 400 μs, the ignition delay begins to increase until a dwell of 200 μs. It then decreases slightly for a dwell of 180 μs, but increases dramatically as dwell decreases further.

The injection rate data shown in Fig. 6 suggest that the shape of the main injection rise rate changes with changing dwells. Of particular interest are the rate shapes for dwells of 300 μs and shorter, as the combustion noise changes significantly over this range of dwells. A separate test was performed with the HDA for a variety of dwells and constant main injection energizing times (as opposed to a variable main injection energizing time to maintain the desired load). The resulting injection rate traces are plotted against time after the start of solenoid energizing (ASSE) of the pilot injection in Fig. 9.

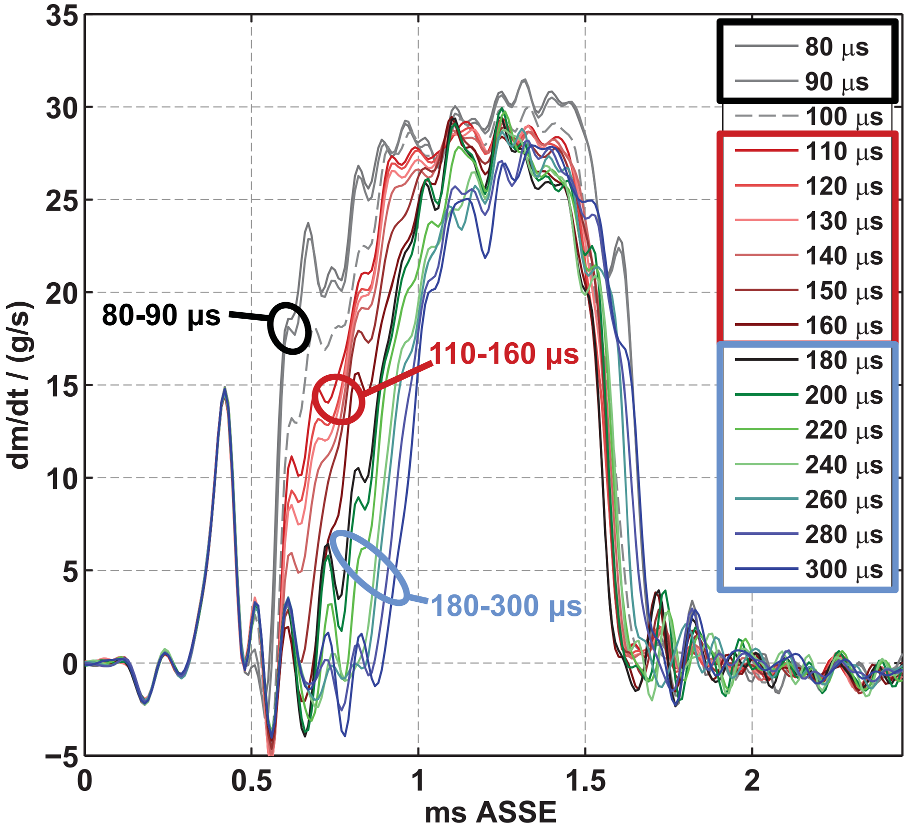

Fig. 9: Injection rates for constant main injection energizing time parameterized by dwell

As expected, the rate shape of the pilot injection is unaffected by changes in dwell. However, as dwell increases from 80 μs, the main injection rise rate transitions through three distinct regimes: a very rapid rise rate at the shortest dwells; a rise rate similar to a single injection for intermediate dwells; and a rise rate that is delayed but with a slightly enhanced rise rate compared to the single injection for longer dwells. The transitions between these regimes occur abruptly; a change in dwell of 20 μs can have a significant impact on the main injection rise rate shape. Dwells of 80 and 90 μs result in main injection rate shapes that are nearly identical.

Because the injection trains shown in Fig. 9 are phased according to the start of solenoid energizing for the pilot injection, they do not convey how the injection train timing would need to be changed to maintain combustion phasing in the engine. Rates of injection as they occur in the engine are presented in Fig. 6, but the main injection rise rate behavior is difficult to see. The main injection rate traces are shown more clearly in Fig. 10, along with the injection rate of the single injection and the solenoid energizing currents for each operating point.

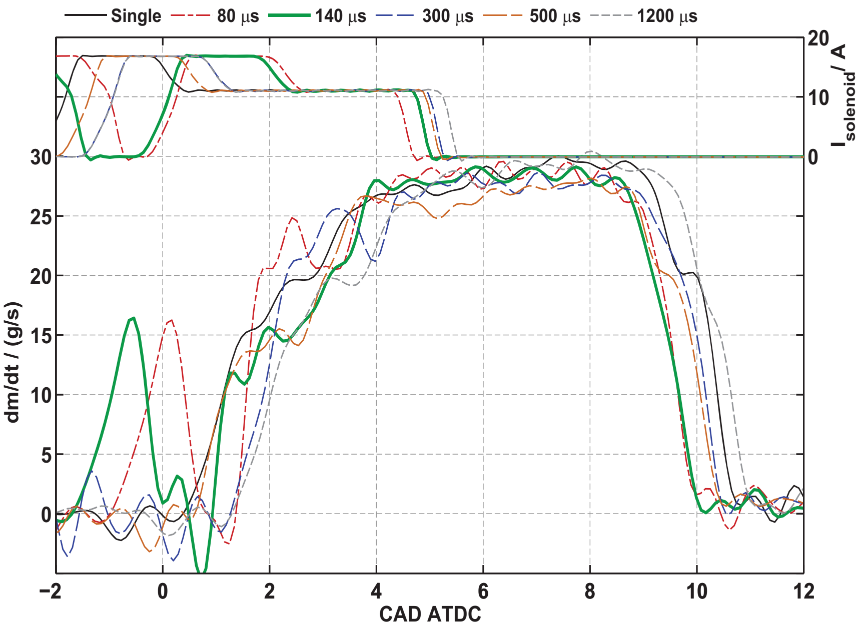

Fig. 10: Injection rates (bottom) and solenoid energizing currents (top) for various dwells and for a single injection

As indicated in Fig. 9, the main injection rise rate for a dwell of 80 µs is the steepest of all dwells tested. Compared to the single injection, the rise rate for a dwell of 140 µs is slightly more intense for the initial stage of the injection, but less intense during the latter part of the initial increase. The main injection rise rate for a dwell of 500 µs, however, is very similar to the rise rate for a dwell of 140 µs. The rise rate for a dwell of 1200 µs starts later than for other dwells and is comparable to the single injection rise rate. The trends described here do not correspond to the combustion noise trends shown in Fig. 4.

Because the three regimes identified in the main injection rate shape (shown in Fig. 9) occur at dwells that seem relevant for the trend in combustion noise (see Fig. 4), optical measurement techniques were applied in the engine to search for evidence of main injection rate shaping. The following operating points were chosen to be investigated with the high-speed elastic scattering measurements:

- Dwell of 90 µs
- Dwell of 140 µs
- Dwell of 300 µs
- Single injection

The simplest information to extract from the imaging data are the optically detected starts of injection. These are compared to the starts of injection as measured by the HDA and shown relative to the start of solenoid energizing (SSE) for the pilot and main injections (denoted with subscripts “p” and “m”, respectively) in Table 3. For every dwell tested, the start of the main injection could clearly be identified in the imaging, thus confirming that even for very short dwells, the pilot and main are separate injection events (cf. Fig. 10). Data for the single injection are omitted, as they are essentially the same as for the pilot injection.

Table 3: Starts of injection as measured by the HDA and detected in imaging data

Dwell (µs)	$SOI_{p,HDA}$ (µs $ASSE_p$)	$SOI_{p,images}$ (µs $ASSE_p$)	$SOI_{m,HDA}$ (µs $ASSE_m$)	$SOI_{m,images}$ (µs $ASSE_m$)
300	311	342	289	320
140	310	342	139	155
90	308	342	170	185

The delay between the start of solenoid energizing and the detected starts of injection are nearly constant for the pilot injection. The start of injection as detected by the HDA occurs sooner than the optically detected start of injection; the time difference between these two events is nearly constant and on the order of 30 µs. For the main injection, the delay between SSE and SOI is smaller than for the pilot for dwells shorter than 300 µs; this trend is observed both with the HDA and with the optical data. For a dwell of 140 µs, this delay is shorter than for the other dwells tested. However, the injection train is block-shifted to achieve the desired combustion phasing for each dwell so this delay is insignificant. The difference in delay times between HDA data and imaging data is smaller for dwells less than 300 µs.

Liquid penetration lengths are computed from the imaging data as described in the appendix for each of 45 cycles. The temporal development of the liquid length measured at one jet is shown in Fig. 11 for each cycle, as is the ensemble-averaged liquid length. Aside from an anomaly at the beginning of the pilot injection that is related to limitations of the background subtraction routine, the liquid penetration behaves nearly linearly for the rise rate of both injection events. This rise rate behavior is highly repeatable for both injections for all cases tested.

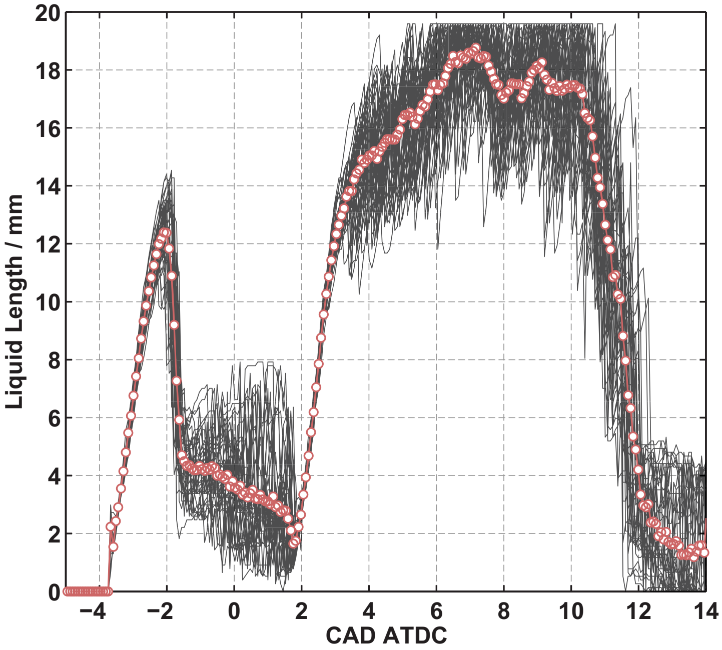

Fig. 11: Liquid lengths for individual cycles (black) and ensemble averaged (line with circle markers) for a dwell of 300 µs

The initial linear liquid penetration is consistent with the short-time behavior of a diesel jet as described in (Naber and Siebers, 1996) and measured by others, for example Hiroyasu and Arai (1990) and Reitz and Bracco (1979). The initial liquid penetration rate of the pilot injection is comparable to the data shown in (Payri *et al.*, 2008) for a similar ambient density, rail pressure, and nozzle hole size. For some cycles, the penetration of liquid fuel extends past the edge of the image. This is evidenced in Fig. 11 by clipping of the individual cycles. As a result, the ensemble-averaged liquid length is not accurate for crank angles between approximately 5 and 11 CAD ATDC. The computed liquid lengths after the initial pilot injection penetration and before the start of the main injection fluctuate from cycle to cycle. This is due to liquid fuel that either dribbles from the injector or to remaining liquid fuel near the injector. The liquid jet penetration behavior is not the same for every jet; some are characterized by shorter pilot injection liquid lengths and wider pilot injection spreading angles. These differences typically become smaller for the main injection. One such jet is chosen for comparison between the various dwells, but the general trends observed in liquid penetration are similar for other jets, particularly during the main injection rise rate. The ensemble-averaged liquid lengths are compared in Fig. 12 for each dwell tested and for the single injection.

The liquid length behavior for the pilot injection does not appear to change as dwell is varied. The end of the pilot injection is characterized by a contraction in liquid length, and for the dwell of 300 µs, the measured liquid lengths become noisy and erratic during the hydraulic dwell. This behavior is attributed to the background subtraction routine, as no liquid fuel is observed in this region of the image at this time. As the main injection starts, the liquid length again increases, and the rates of these increases appear to be different for each dwell. After the rise rate phase, the liquid length behaves similarly for all of the dwells.

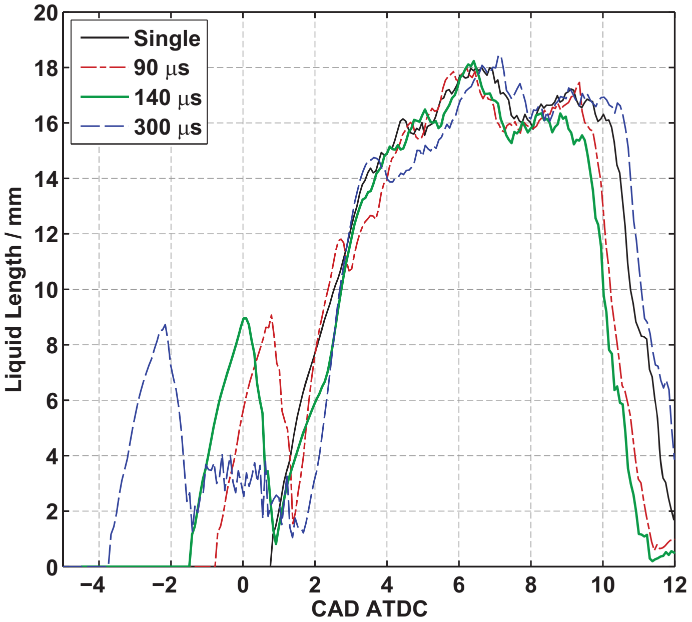

Fig. 12: Liquid length comparison for a single jet with dwell as a parameter

In order to characterize the differences in the liquid length behavior during the first phase of the main injection, the time derivative of the liquid length curves is calculated and averaged over all seven jets. The resulting penetration rate curves are shown in Fig. 13. Note that the injection rate shape is shown for a dwell of 80 μs, whereas the penetration rate is shown for a dwell of 90 μs; the injection rate shapes shown in Fig. 9 suggest that the differences in rate shapes between these two dwells are minimal. Only positive penetration rate values are shown in Fig. 13.

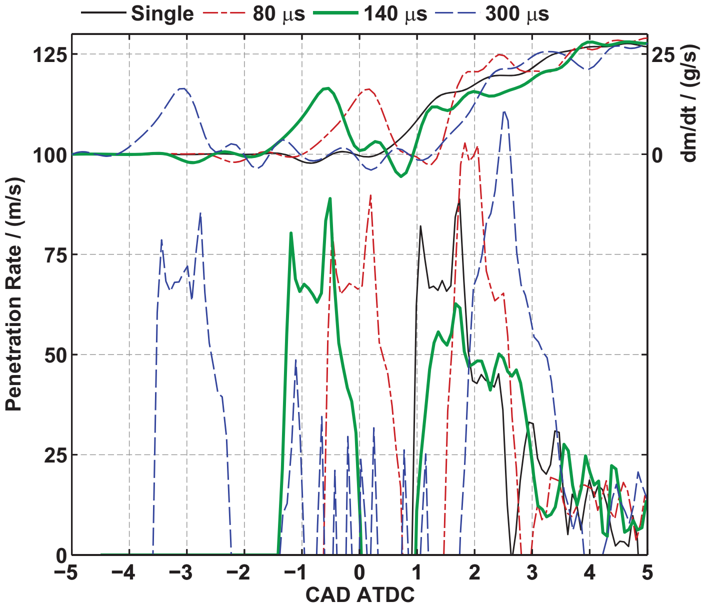

Fig. 13: Optically-measured liquid penetration rate and rate of injection as measured by the HDA with dwell as a parameter

The shape of the optically-measured jet penetration rate curves for the pilot injection events are very similar to one another and to that of the single injection. The phasing of the pilot injection penetration rates relative to their corresponding injection rate profiles (measured with the HDA) is consistent for each dwell. As indicated by the rate of injection data (HDA), the single injection begins at a crank angle before any main injections, followed by the main injection for a dwell of 140 µs. This behavior is also observed in the (optical) penetration rate data. However, optical data indicates that the main injection for a dwell of 90 µs begins at an earlier crank angle than for a dwell of 300 µs. This does not agree with the trend shown in the HDA data. The peak main injection penetration rates (optical) for a dwell of 140 µs are lower than for any other case; this behavior is consistent with the lower rates of injection (HDA) for this dwell. The phasing and amplitudes of the maxima in the penetration rates agree qualitatively with the corresponding trends in the injection rate data.

4. Discussion

The comparison between rates of injection as measured by the HDA and the optically-determined jet penetration rates provides strong evidence that injection rate shaping of the first phase of the main injection is occurring, and that this rate shaping changes as dwell changes. The qualitative agreement between these two data sets lends credibility to the rates of injection measured outside the engine with the HDA.

When taken alone, the data shown in Fig. 13 provide evidence that the rate shaping of the main injection may play a significant role in the combustion noise trend shown in Fig. 4. However, if all of the main injection rate shapes measured by the HDA are representative of the true injection rate behavior during fired engine operation, then significant evidence exists to refute this claim. For example, Fig. 10 shows that the main injections for dwells of 80 µs and 1200 µs begin at nearly the same crank angle. The rates of injection increase much faster and reach higher levels for the dwell of 80 µs, and indeed the AHRR data for these two dwells (shown in Fig. 6) are significantly different from one another. However, the combustion noise for a dwell of 80 µs is only 0.4 dB louder than for a dwell of 1200 µs, which equates to a factor in acoustic power of approximately 1.1. Furthermore, the injection rate shapes for dwells of 140 µs and 500 µs are very similar. Differences in the AHRR behavior of these two dwells exist, but they are certainly less significant than for the comparison between 80 µs and 1200 µs. In the 140-500 µs dwell comparison, the difference in combustion noise is approximately 3 dB, which is a factor of two in acoustic power and much more significant that the noise difference between the cases of 80 µs and 1200 µs. These results are not consistent with the notion that main injection rate shaping can significantly affect combustion noise. We do not have evidence to suggest that the rates of injection measured by the HDA are inaccurate. Rather, the optical measurements promote confidence in the accuracy of the HDA results. It is hypothesized that in this case, the combustion noise trend is caused primarily by other factors.

One such factor may be the result of the interaction between the pilot mixture field and the main injection. The lower peak rates of pilot heat release for a dwell of 140 µs, combined with the temporal overlap between the pilot heat release and the main injection (see Fig. 6), support the theory that the main injection can influence the pilot mixture combustion process. The abrupt increase in ignition delay for dwells shorter than 180 µs shown in Fig. 8 provides further evidence that the main injection can interfere with the ignition process of the pilot mixture. The resulting decrease in peak pilot mixture heat release rates may play a role in creating the combustion noise minimum observed for a dwell of 140 µs.

As dwell is changed through a large range of values, it is conceivable that the way in which the main injection mixture field is ignited or inflamed also changes. Computational modeling presented in (Hasse and Peters, 2005) indicates that a premixed, near-stoichiometric, strained flame propagates through the pilot mixture field and towards the main injection mixture field. The associated transfer of heat and mass between the two mixture fields is ultimately responsible for the ignition of the main injection mixture field. Large mixture fraction gradients in the pilot mixture field increase the propagation speed of the premixed flame, thus shortening the inflammation delay for the main injection mixture field. The timing of the main injection relative to the pilot injection was not discussed in this work, but it would most certainly change the way in which these two mixture fields interact.

Another factor that may contribute to the observed trend in combustion noise is the effect of the changing relative phasing between the pilot and main injection heat release. Initial results indicate that this phasing change could be a significant, if not dominant factor; it must therefore be the subject of future studies.

5. Summary

A sweep of pilot-main energizing dwell was performed in a small-bore, light-duty Diesel engine at a moderate engine load. Dwell varied between 1200 µs and 80 µs as engine load and combustion phasing (MFB50) were held constant; a minimum in combustion noise was recorded for a dwell of 140 µs without a penalty in pollutant emissions. The injection schedules used during the engine testing were evaluated offline using the fuel injection equipment together with an injection rate measuring device. Optical scattering measurements at 120 kfps were made in the engine with motored (non-combusting) operation to examine the injection behavior at several dwells and processed using an automated image distortion correction routine based on ray tracing to determine liquid length and liquid penetration rates.

Both the rate of injection results and the calculated jet penetration rates suggest that rate shaping of the first phase of the main injection is occurring in the engine (see Fig. 10 and Fig. 13), and the trends in these data agree qualitatively. However, the lack of clear correlation of both heat release data and measured rates of injection with combustion noise does not support the idea that main injection rate shaping is responsible for the significantly lower combustion noise levels measured at dwells near 140 µs. These data suggest that the main injection and the (possibly combusting) pilot mixture field do interact, and the resulting impact on the heat release associated with the pilot injection may play a role in creating the observed minimum in combustion noise. Additionally, the relative phasing of the pilot and main heat release is believed to play a significant role in determining combustion noise for close-coupled pilot injections. In this work, we’ve shown that with an optimized pilot-main injection strategy, combustion noise can be reduced by 3 dB compared to non-optimized pilot-main strategies with no emissions penalty.

Acknowledgements

The authors thank Ethan Eagle and Jeremie Dernotte for their insightful comments on this work. Support for this work was provided by the United States Department of Energy (Office of Vehicle Technologies) and by General Motors Corporation (agreement FI083070326). This work was performed at the Combustion Research Facility of Sandia National Laboratories in Livermore, California. Sandia is a multiprogram laboratory operated by Sandia Corporation, a Lockheed Martin Company, for the United States Department of Energy’s National Nuclear Security Administration under contract DE-AC04- 94AL85000.

References

Badami, M., Millo, F., and D'Amato, D., "Experimental Investigation on Soot and NOx Formation in a DI Common Rail Diesel Engine with Pilot Injection," SAE Technical Paper 2001-01-0657, 2001, doi:10.4271/2001-01-0657.

Diesel Systems: Common Rail Systems CRS2 with 1,600 to 2,000 bar and solenoid injectors. Robert Bosch GmbH, Diesel Systems, 2011. Available online March 2014.

Dürnholz, M., Endres, H., Frisse, P., “Preinjection A Measure to Optimize the Emission Behavior of DI-Diesel Engine,” SAE Technical Paper 940674, 1994, doi:10.4271/940674.

The new 1.3 Multijet II 95 HP (Euro5) engine is making its first appearance on the Fiat 500 and 500C. Fiat Group Automobile Press, 25 Nov. 2009. <www.fiatgroupautomobilespress.com/cartelle/zoom/4594>, Available March 2014.

Hasse, C., Peters, N., “Modelling of ignition mechanisms and pollutant formation in direct-injection Diesel engines with multiple injections,” International Journal of Engine Research, Vol. 6, No 3, pp. 231-246, June 1, 2005.

Hiroyasu, H. and Arai, M., "Structures of Fuel Sprays in Diesel Engines," SAE Technical Paper 900475, 1990, doi:10.4271/900475.

McFarlane, N.J.B., Schofield, C.P., “Segmentation and tracking of piglets in images,” Machine Vision and Applications, Vol. 8, Issue 3, pp. 187-193, 1995.

Moehwald HDA instruction manual: “Injection analysis using the method of hydraulic increase of pressure.” Moehwald GmbH, Sept. 24, 2008.

Naber, J. and Siebers, D., "Effects of Gas Density and Vaporization on Penetration and Dispersion of Diesel Sprays," SAE Technical Paper 960034, 1996, doi:10.4271/960034.

Payri, R., Salvador, F.J., Gimeno, J., de la Morena, J., “Macroscopic Behavior of Diesel Sprays in the Near-Nozzle Field,” SAE Int. J. Engines, Vol. 1, Issue 1, 2008; SAE technical paper 2008-01-0929.

Reitz, R. and Bracco, F., "On the Dependence of Spray Angle and Other Spray Parameters on Nozzle Design and Operating Conditions," SAE Technical Paper 790494, 1979, doi:10.4271/790494.

Ricaud, J.C. and Lavoisier, F., “Optimizing the multiple injection settings on an HSDI diesel engine,” Proceedings of the Conference on Thermo- and Fluid-Dynamic Processes in Diesel Engines, pp. 251-275, Valencia, 2002.

Russell, M., Young, C., and Nicol, S.W., "Modulation of Injection Rate to Improve Direct Injection Diesel Engine Noise," SAE Technical Paper 900349, 1990, doi:10.4271/900349.

Shahlari, A., Hocking, C., Kurtz, E., and Ghandhi, J., "Comparison of Compression Ignition Engine Noise Metrics in Low-Temperature Combustion Regimes," SAE Int. J. Engines 6(1):541-552, 2013, doi:10.4271/2013-01-1659.

Smith, W.J., Modern Optical Engineering, 4th ed., McGraw-Hill, New York: 2008.

Zeuch, W., „Neue Verfahren zur Messung des Einspritzgesetzes und der Einspritz-Regelmäßigkeit von Diesel-Einspritzpumpen.“ MTZ Vol. 22, Issue 9, 1961.

Appendix: Image Distortion Correction and Processing

Because imaging is performed through the piston, the raw images are distorted. The distortion pattern depends on both the crank angle and the location of the object plane relative to the piston. While automatic distortion correction routines exist in commercial image capture software packages, they often require human intervention if the distortion becomes too extreme. For this work, a new approach to automated image distortion correction has been developed based on ray tracing. This approach takes advantage of the axisymmetry of the piston (except for the valve cut-outs, which do not affect images of the fuel injection), so the problem of distortion correction is reduced to two dimensions (a radial dimension and a dimension parallel to the cylinder axis). The simulation of rays and their interaction with the piston is simulated with the methodology described below.

A ray is defined by its starting point and direction of propagation. The intersection of the ray's path and a surface is computed and the interaction of the ray with the surface simulated. Depending on the nature of the surface, the ray may be reflected, refracted, or absorbed. It is then transformed into a new ray (defined by its origin at the intersection and its new direction). Refraction is computed according to Snell's law (Smith, 2008).The ray is traced in this manner until it leaves the system. Cubic splined surfaces with continuous first derivatives define the two-dimensional piston perimeter (shown in Fig. 14).

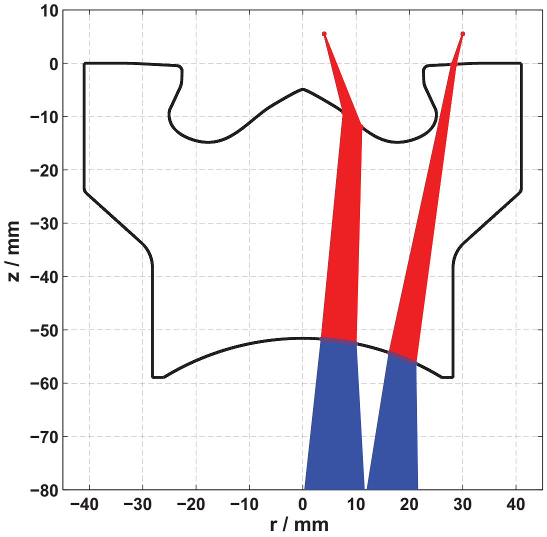

Fig. 14: Ray bundles originating from two points in 2-D space above the piston and their paths through the piston towards the mirror

A fan of rays with their origins at a given point in space above the piston is defined, and each is traced until it leaves the system. The rays that determine the form of the distorted image are those that reach the piston mirror and camera. In the case of this simulation, these rays are assumed to be the ones that pass through a long (~250 mm) absorptive vertical tube (diameter 49.8 mm) located below the piston so that they reach the elliptical piston mirror (depicted in Fig. 3). The ray bundles shown in Fig. 14 represent the rays that leave from these two original points and reach the piston mirror. Rays leaving these points at any other angle will not reach the mirror. In other words, only rays that would reach the piston mirror are allowed to leave the system. It is observed that the rays leaving the piston and reaching the turning mirror are divergent (shown by the bundles of rays leaving the bottom of the piston in Fig. 14). Therefore, one or several virtual images are formed at the back-projected intersections of these rays with one another. In this way, a point in real space is mapped to a cloud of intersection points that are the virtual image of the original point. The virtual images of objects above the piston (calibration targets, liquid fuel, etc.) are what the camera "sees".

For crank angles near TDC and ray fan origins in or near the piston bowl, the virtual images that form are often confined to very small spaces, such that they can be represented by a single point with reasonable precision (typically better than 100 μm in the radial direction). For this work, a mapping between the real world and the virtual image is defined in this manner. A series of ray fans located at various points along a line inside the cylinder can be traced and represent the radial mapping function of a surface in real space. Once this mapping function is known, an image is distortion-corrected as follows:

1. The center of the cylinder is determined from the raw (distorted) image; this is performed manually, as the location of the center does not change from experiment to experiment.
2. The distance between the center point and each pixel (i.e. radius) in the raw image is computed.
3. The radii determined in step 2 are scaled by an empirically determined scaling factor (the ratio of distance in virtual image space to pixels in the captured images) to determine their magnitude (in mm).
4. The virtual image radii are used as inputs to the radial mapping function to yield undistorted radii.
5. The undistorted radii are scaled by a constant (8 pixels/mm) to determine the spatial scaling of the final image.
6. The pixels of the original image are moved into their new positions as defined by the undistorted radii (the angular position of each pixel remains unchanged).
7. A two-dimensional, bi-linear interpolation scheme is used to “fill in the blanks”, that is the locations where no information is available after the initial pixel displacement procedure described in step 6.

It is observed that the distortion of a horizontal plane changes dramatically as the plane is moved parallel to the cylinder axis towards the piston pip. This is a problem when imaging the injection jets, as they are not oriented in a horizontal plane. Ray tracing is therefore performed for ray fans located along the theoretical jet axis (inclined by 15.5 ° to the cylinder head). An example of such a ray tracing simulation is shown in Fig. 15 for a limited number of ray bundles. The black dots indicate the locations of the virtual images of each point along the jet axis. Mapping functions generated in this manner are created for crank angles between 12 CAD BTDC and 30 CAD ATDC in increments of 2 CAD. They are combined in three-dimensional space (crank angle, virtual image radius, undistorted radius) and a surface is fitted to them. This surface is used to determine the mapping function (via bilinear interpolation) for any arbitrary crank angle within this range. In this way, any image can be automatically distortion corrected if the crank angle at which it was taken is known.

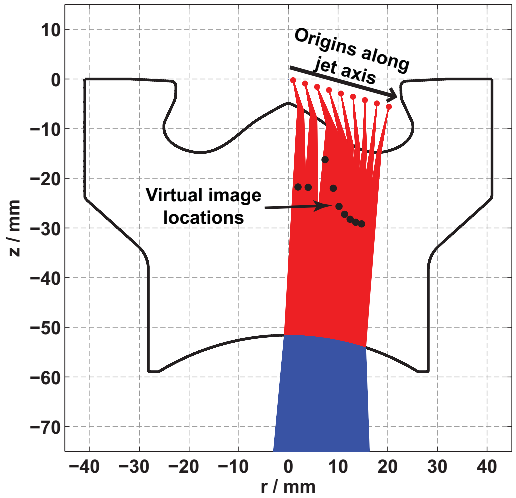

Fig. 15: Example of ray tracing with ray bundle origins located along the injection jet axis and black dots to show the locations of virtual images

For this work, the distortion corrected images are scaled to a resolution of 8 pixels per mm along the jet axis. Testing of this procedure with calibration targets oriented along the jet axis indicate that it introduces an uncertainty in liquid length measurements of something on the order of 2 pixels, or 0.25 mm along the jet axis. However, any errors in liquid length measurements will be largely consistent between different cases, as the distortion correction is the same for a given crank angle. This facilitates comparison between images taken for various dwells.

Once the images in a sequence have been distortion corrected, steps are taken to isolate the injection jets from the background. For this work, the approximate median method described in (McFarlane and Schofield, 1995) is used to model the background. This method relies on a sequence of images, which in this case are the sequences of 300 distortion corrected images for every injected cycle. The background model is initialized as the first image (taken at SSE, at which point the injection has not yet started). For each subsequent image in the sequence, the background model is updated and a background subtracted image is created, then thresholded. This method effectively removes features attributed to the background, such as the valves and the injector tip. Finally, each jet's image data is isolated and processed individually. Liquid lengths are calculated according to the methods given by Naber and Siebers with some subtle differences (1996). Liquid lengths are initially computed from the images and are measured from the empirically determined center of the chamber (not the apparent origin of the jet, which cannot be adequately distinguished from the injector's axis with the resolution provided by this system). The distance between the injector axis and the nozzle exits is subtracted from this distance. This length represents the projection of the true liquid length, which exists along the jet axis, onto a horizontal plane. The liquid lengths reported in this work are calculated by dividing this length by the cosine of 15.5 °. A threshold value of 3% of the maximum intensity for the jet in question proved to be robust for all cases. Liquid lengths are calculated for each jet in each frame in every image sequence. An example of a distortion corrected, background-subtracted image is shown in Fig. 16. The locations where the projected liquid length is computed are shown with small "+" symbols, and a large "+" is positioned at the center of the image.

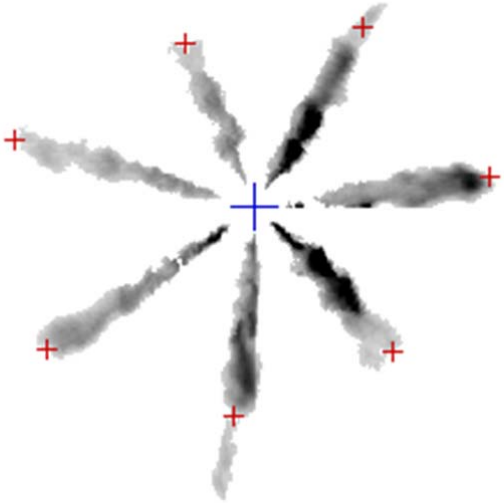

Fig. 16: Distortion corrected, background-subtracted image; displayed with an inverted grayscale color map, 0-512 counts, gamma = 0.7

The visually detected starts of injection events are defined by the frame for a given operating point at which bright spots at the injector nozzle holes are visible in every cycle. For the preceding frame, these bright spots are visible only for some cycles, so there is some scatter in the visually detected start of an injection event. This scatter never involves more than two frames, so the combined temporal uncertainty and scatter in the visually detected start of injection are on the order of 15 μs.